

Size Dependent Anisotropic Strain and Optical Properties of Strained Si Nanocrystals

Soumen Dhara¹ and P. K. Giri^{1,2,*}

¹Department of Physics, ²Centre for Nanotechnology, Indian Institute of Technology Guwahati, Guwahati 781039, India

We report on the growth of strained Si nanocrystals (NCs) of sizes in the range 5–43 nm and analyze the detailed nature of strain and its influence on the optical properties of the NCs as a function of size. Freestanding Si NPs were prepared in a controlled way using a contamination free mechanical ball milling for duration 2–40 hrs. Structural analysis based on X-ray diffraction (XRD) pattern and high resolution transmission electron microscopy (HRTEM) confirms the good crystalline nature of these Si NCs. A detailed analysis of XRD line profile reveals that nature of the strain is anisotropic and the screw type dislocations are the main contributors to the lattice strain. The dislocation density and corresponding strain changes non-monotonically, while the crystallite size changes monotonically with milling time. Direct evidence of dislocations is shown from HRTEM images. The UV-vis-NIR absorption spectra of the Si NCs show an enhanced absorption band in the visible region that shows a systematic blue shift with reduced NC sizes. Si NCs with size ~5–10 nm exhibits a distinct photoluminescence (PL) band in the visible region at 580–585 nm at room temperature, while higher size NCs does not exhibit any visible emission. PL excitation measurement shows a very small Stokes shift for the visible emission band indicating no involvement of defects/interface in the emission. We argue that the observed absorption and emission can be explained based on the enhanced confinement effect on the strained Si NCs due to the combined effect of strain and size quantization.

Keywords: Si Nanocrystals, Anisotropic Strain, Photoluminescence, XRD Line Width.

1. INTRODUCTION

Si nanocrystals (NCs) are most potential class of material for their unusual quantum induced electronic and optical properties. Although Si is an indirect bandgap semiconductor, Si NCs show photoluminescence (PL) in the visible (green-red) region. The origin of the visible PL in the Si NCs is still under debate, although much of the present controversy arises due to difficulty in isolating the contribution of quantum confinement,¹ surface states² and embedding matrix have on the band structure in these materials. For a detailed understanding of their size dependent electronic and optical properties, free standing Si NCs with controlled size is essential. In majority of the growth methods, Si NCs are frequently embedded in or grown on other materials with different elastic constants and lattice parameters. In such a case, due to the lattice mismatch, the consequent elastic strain within the NCs is known to impact their electronic structure and hence optoelectronic properties.³ Strain can shift the valence and

conduction bands, change band gap, cause trapping of carriers and excitons, shift the oscillator strength of indirect-bandgap clusters.⁴ Peng et al.³ studied the effect of strain on the band gap of small Si clusters (<2 nm) through density functional calculation and emphasized the role of surface passivation for small clusters. Lyons et al.⁵ studied the tailoring of the optical properties of embedded Si nanowires through strain. Thean and Leburton⁶ studied the strain effect in Si NCs (10 nm) embedded in SiO₂ and showed that coupling between the NC-Si geometry and the symmetry generated by the strain potential can enhance confinement in the quantum dot. Thus, one would expect an enhanced quantum confinement effect resulting in an increased band gap for strained Si NCs as compared to the unstrained Si NCs.

Several groups reported the role of strain and quantum confinement on optical emission of semiconductor NCs. Examples include strained Si NCs embedded in a SiO₂ matrix^{6–7} and InAs dots embedded in In_xGa_{1–x}As layers.⁸ Li et al.⁹ reported an enhanced PL from strained Ge with δ -doping of SiGe layer on Si and Si-on-insulator. While these studies find evident strain effects on the band gap, to

*Author to whom correspondence should be addressed.

our knowledge no study has focused on the coupled effects of size and strain on the optical properties of Si NCs.

In this work, we prepared ultra fine freestanding Si NCs with size down to ~ 5 nm using ball-milling method and systematically investigated the strain evolution and changes in optical properties of the strained Si NCs as the function of size. Morphology and microstructure of the Si NCs are studied by high resolution transmission electron microscopy (HRTEM). Si NCs size and strain are calculated from details analysis of X-ray diffraction (XRD) line profile using Williamson-Hall (WH) method¹⁰ and the method proposed by Unger and Borbely.¹¹ The optical properties are studied at room temperature by UV-vis-NIR absorption and PL measurements. Origin of visible PL and enhanced optical absorption is discussed in the framework of strain potential and quantum size effects on Si NCs.

2. EXPERIMENTAL DETAILS

Freestanding Si NCs are prepared from commercially available Si powder with average particle size $\sim 75 \mu\text{m}$ (Sigma Aldrich, >99% purity) using mechanical ball milling method. Ball-milling was performed at 450 rpm for duration up to 40 hours in a zirconium oxide vial (Restch, PM100) under atmospheric pressure and temperature. Small zirconium oxide balls were used for the ball-milling and this ensured contamination-free milling process. The ball to Si powder weight ratio was taken as 20:1. Very fine Si NCs with few nanometer sizes were obtained after milling. The nanopowder was taken out for measurement after 2, 5, 10, 20, 30 and 40 hours of ball-milling. After the milling, the powder samples were analyzed by powder XRD (Seifert 3003 T/T) using Cu K_{α} radiation. For careful determination of average nanocrystals size, internal lattice strain and dislocation density, XRD data was collected at a slow rate at of 0.0025° per second. The size, strain and related dislocation density were calculated by employing WH plot¹⁰ and the Unger et al. method.^{11,12} A 200 kV HRTEM (JEOL, JEM-2100) was used to study the size distribution, morphology and microstructure of the freestanding Si NCs. The UV-vis-NIR absorption spectra of all the samples were recorded using a commercial spectrophotometer (Shimadzu 3010PC). Room temperature PL and PL excitation measurements were performed by using a commercial Fluorimeter (Thermo Spectronic, AB2) with a monochromated xenon lamp source.

3. RESULTS AND DISCUSSION

3.1. XRD Line Profile Analysis and Anisotropic Strain

The XRD patterns of the freestanding Si NCs obtained after different duration of milling is shown in the Figure 1, along with the XRD pattern of unmilled Si powder. All the

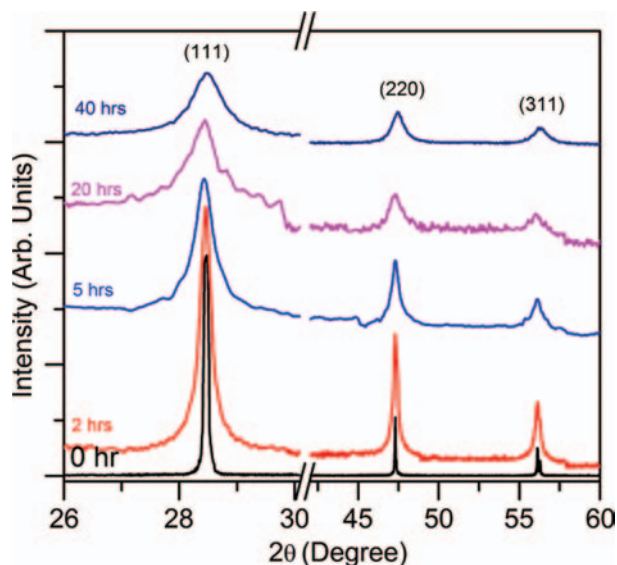


Fig. 1. XRD pattern of the unmilled Si powder and milled Si NCs showing gradual broadening of the peak with increasing milling time. The peak broadening arises from size reduction and strain in the Si NCs.

milled Si NCs show strong characteristic XRD peaks for the Si(111), (220) and (311) planes. Therefore, prepared Si NCs have good crystalline nature. It is observed that full width at half maximum (FWHM) of these peaks gradually increased with increasing milling time. This peak broadening confirmed the size reduction and development of strain in the NCs.¹³ The lattice spacing (d_{111}) of the Si NCs is also reduced compared to the strain free lattice spacing of Si. The d_{111} values are in the range $3.11\text{--}3.12 \text{ \AA}$ for different hours milled Si NCs, which are marginally lower than the spacing expected from unstrained Si crystals (3.13 \AA). Thus, a compressive strain may be present in the Si NCs. The FWHM of each of the XRD peak was carefully analyzed by fitting a Lorentzian line shape to the experimental data points. Instrumental broadening is subtracted from the fitted FWHM value for line shape analysis. Apart from characteristic XRD peak of Si, no other peak related to Si oxide or any contaminant material was detected in XRD spectra, even for data acquisition at very slow scan rate. This implies that Si nanocrystals are not embedded in any matrix and free from any substantial contamination. However, presence of ultrathin amorphous oxide phase cannot be fully ruled out. Note that earlier study by Shen et al.¹⁴ showed the presence of oxide phase by gas fusion principle on the Si NCs after ball-milling.

As ball-milling process easily introduces strain in the as prepared NCs, the WH method¹⁰ is used to isolate the contribution of strain and NCs size in the peak broadening in XRD pattern. According to WH method, the individual contribution of the NCs to the XRD peak broadening can be expressed as

$$\beta \cos \theta = 0.9\lambda/D_{\text{WH}} + 4\varepsilon \sin \theta \quad (1)$$

where β is the FWHM of the Bragg peaks (in radians), θ is the Bragg angle of the analyzed peak, λ is the wavelength of the X-ray ($\lambda = 0.154056$ nm for Cu K_α), D_{WH} is the average crystallite size and ε is the strain. The XRD peaks corresponding to Si(111), (220) and (311) planes were used to draw a linear plot of $\beta \cos \theta$ versus $\sin \theta$ according to WH method. Due to inappropriate fit shown in Figure 2(a), the calculated sizes and strains are very large compared with the sizes obtained from TEM analysis. Further, error bar is very large due to scattered data in the WH plot. The divergences are larger when the studied material has some anisotropic strain, because the effect of anisotropic strain on a particular Bragg reflection is different from other. If the anisotropy of strain is not considered, calculated average particle size and strain using Eq. (1) is shown in Figure 2(b) as a function of milling time. It is apparent from Figure 2(b) that average NC size gradually decreases with increasing milling time. On the other hand, the lattice strain first increases with milling time and reached saturation after 10–20 hours of milling and then it reduces with further milling. However, estimated sizes of NCs are much larger than the actual size measured by TEM, as shown later.

For a better linear fit to the WH plot, Ungar et al.¹¹ method was followed that suggested the introduction of a dislocation contrast factor in Eq. (1) to take into account the anisotropy of strain. According to the Ungar et al. method,¹¹ Eq. (1) can be expressed as

$$\Delta K = 0.9/D_U + 2eK\sqrt{C} \quad (2)$$

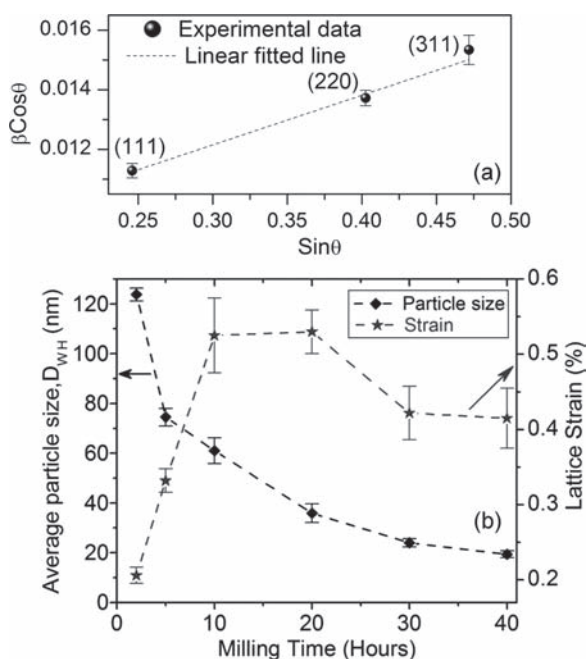


Fig. 2. (a) Representative WH plot for 40 hours milled Si NCs. The experimental data points (symbols) are shown with a linear fit (dashed line) showing a poor fit to the data. (b) Average particle size (D_{WH}) and lattice strain (ε) as a function of milling time as calculated from above WH plots.

where $\Delta K = (2\beta \cos \theta_B)/\lambda$, β is the FWHM (in radians) of the Bragg reflections, λ is the wavelength of X-rays, D_U is the average crystallite size, $K = 2 \sin \theta_B/\lambda$, e is the strain and C is the dislocation contrast factor, respectively. The term, $2eK\sqrt{C}$ is considered as the strain contribution to the line broadening. The term C in Eq. (2) explicitly contains the anisotropy factor. The dislocation factor can be determined by the elastic anisotropic factor and the dislocation type of the material.¹² For dislocated crystals, ΔK can be simplified to Ref. [12]

$$\Delta K \cong 0.9/D_U + \sqrt{(\pi b^2 \rho / (2B))} K \sqrt{\bar{C}} \quad (3)$$

where b is the modulus of Burgers vector of dislocations, ρ is the average dislocation density, \bar{C} is the average contrast factor and B is a constant. The constant B is taken as 10 for wide range of dislocations.¹² For cubic crystal average dislocation contrast factor is

$$\bar{C} = \bar{C}_{h00}(1 - qH^2) \quad (4)$$

Where \bar{C}_{h00} is the average dislocation contrast factor of the $h00$ type reflections and $H^2 = (h^2k^2 + h^2l^2 + k^2l^2)/(h^2 + k^2 + l^2)^2$. The values of \bar{C}_{h00} and the q parameter can be calculated numerically for different dislocation type as the functions of the elastic properties of the crystal. For a fcc crystal like Si, the \bar{C}_{h00} depends on elastic anisotropic factor $A_i = 2C_{44}/(C_{11} - C_{12})$ and the ratio of C_{12}/C_{44} where C_{11} , C_{12} and C_{44} are the elastic constants. For Si, the standard value of elastic constants are $C_{11} = 165.7$ GPa, $C_{12} = 63.9$ GPa and $C_{44} = 79.6$ GPa.¹⁵ Ungar et al.¹² has shown the dependence of \bar{C}_{h00} by following equation

$$\bar{C}_{h00} = \alpha[1 - \exp(-A_i/\beta)] + \gamma A_i + \delta \quad (5)$$

where α , β , γ and δ are numerical constants that depends on the ratio C_{12}/C_{44} . For edge dislocations in Si, the calculated values of α , β , γ and δ are 0.15454, 1.79601, 0.01982 and 0.09466, respectively.¹² And for screw dislocation, the calculated values are $\alpha = 0.1740$, $\beta = 1.9522$, $\gamma = 0.0293$ and $\delta = 0.0662$. With these values, \bar{C}_{h00} is found 0.215507 for edge dislocation and 0.207932 for screw dislocation. Thus, average value of $\bar{C}_{h00} = 0.211719$. Now in the combined equation of (3) and (4), the unknown parameters are q , D_u and ρ . The q value is obtained by plotting ΔK versus $K\sqrt{C}$ and adjusting q value in such a way that data points follow a linear fit. In this method, we obtained q values ranging from 0.741 to 1.742 for different duration of milling. The fitted q values obtained for different milling time is presented in Table I. For pure edge type dislocation, $q = 0.73$ and for pure screw type dislocation, $q = 1.72$ in Si.¹² Thus, we find that during the initial stages of milling time both screw and edge type dislocations are formed, while for longer milling time screw type dislocations dominate in the Si NCs.

Considering the anisotropy factor in strain, a representative modified WH plot using Eq. (3) is shown in

Table I. The calculated values of the q parameter derived from fitting of ΔK versus $K\sqrt{C}$ plot for the different duration of milling.

Milling time (hrs)	q values	Average size of Si NCs (nm)
0	—	—
2	1.186	43.0 ± 0.06
5	0.741	29.6 ± 0.05
10	1.511	18.9 ± 0.04
20	0.860	14.5 ± 0.04
30	1.742	10.0 ± 0.03
40	1.549	8.2 ± 0.07

Figure 3(a). Here we obtained a much improved linear fit to the experimental data points. The crystallite size and dislocation density are calculated from slope and intercept of the fitted line, which is shown in Figure 3(b). Due to improved fitting, the error bars in the NCs size are very small and these are in close agreement with the sizes obtained from TEM analyses (as shown in Fig. 3(b) for comparison). It is evident that Si NC sizes monotonically go down from 43 nm to 8.2 nm as the milling time increases from 2 hours to 40 hours. Note that for 40 hours milled NCs, the average size measured from TEM is 6.8 nm, while the size obtained from XRD line profile is 8.2 nm. On the other hand, the dislocation density first increases up to 10 hours of ball-milling and then slowly decreases for higher milling time. The decrease in size

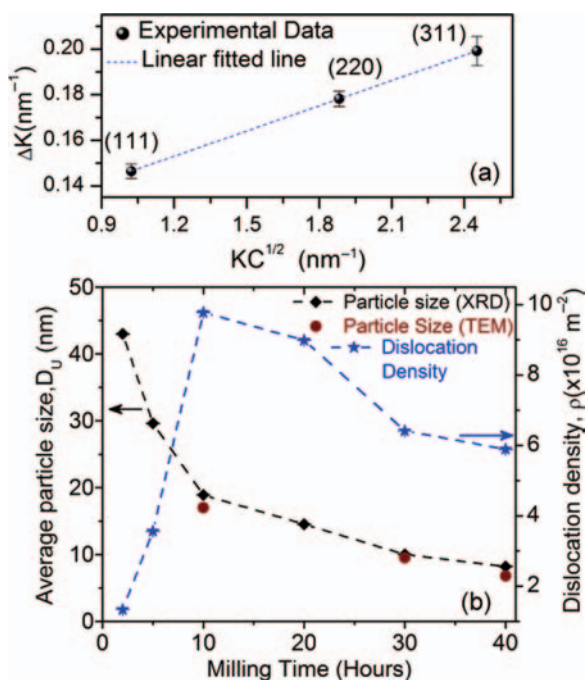


Fig. 3. (a) The modified WH plot using Eq. (3) incorporating contribution of strain anisotropy in the XRD line profile for 40 hours milled Si NCs. The experimental data points (symbols) are fitted with linear (dotted line) function of $KC^{1/2}$. (b) Average particle size (D_U) and dislocation density (ρ) are calculated from the linear fits. For comparison, sizes obtained from TEM images are also shown with solid circles showing close agreement between the two methods.

and increase in dislocation density with increasing milling time is quite expected. However, we notice a decrease in dislocation density after 10 hours of milling. This can be explained as follows: during milling the strain and dislocations first develops, however for prolonged milling when the dislocation density is high the crystal breaks along the slip plane and thus produces smaller size NCs. In this way, strain is partly released for prolonged milling time. Further, there may be possibility of *in situ* heating during the milling. *In situ* heating allows the crystallite to relax the lattice strain and also increase the grain size by grain growth, while milling process will tend to reduce the crystallite size.¹⁶ Thus the reduction in size eventually saturates for prolonged milling for a given set of balls and source material.

3.2. High Resolution TEM Analysis

After 40 hours of milling, we obtained freestanding spherical NCs with sizes in the range 3.5–10 nm, which is shown in the TEM image of Figure 4(a). The inset shows the histogram of the size distribution of freestanding Si NCs

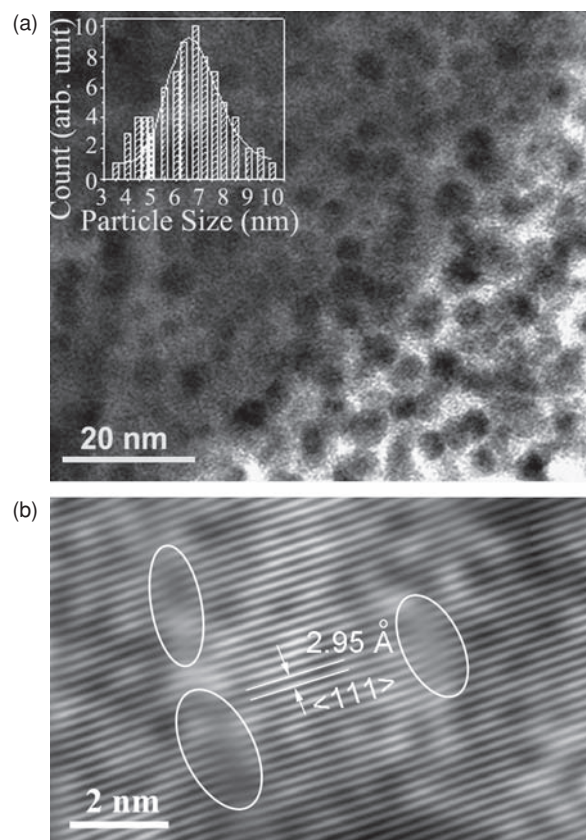


Fig. 4. (a) TEM image of the freestanding Si NCs after 40 hours of milling. Inset shows the histogram of size distribution of the Si NCs. Average size is 6.8 nm as calculated from log-normal fitting (solid line) to the size distribution. (b) HRTEM lattice image of 10 hour milled Si NCs showing distorted lattice (regions marked with oval) due to presence of compressive strain.

measured from the TEM image. The average size of the NCs is calculated to be 6.8 nm from log normal fitting to the size distribution curve. For 30 hrs milling, average NC size is 9.5 nm. Thus, the sizes obtained after 30 and 40 hrs of milling are lower than the exciton Bohr diameter (9.8 nm) of bulk Si crystals. Hence, the quantum confinement effect is expected to play a significant role in determining the optical properties of these NCs. Figure 4(b) is the inverse first Fourier transformed lattice image of a Si NC obtained after 10 hours of milling. Lattice strain (distortion) caused by the dislocations is clearly seen (regions marked with ovals) from the HRTEM image. Analysis of the HRTEM image show that the inter planner spacing $d_{(111)}$ is decreased from 3.13 Å to 2.95 Å, which indicates the presence of a compressive strain. These results are consistent with the XRD line profile analysis discussed before.

3.3. UV-Visible-NIR Absorption Spectroscopy

Figure 5 illustrates the UV-Vis-NIR absorption spectra of different sizes Si NCs. The unmilled Si powder showed featureless absorption spectra in the near IR range (not shown). In contrast, all the Si NCs exhibit enhanced absorption in the green region of the visible spectrum. From the absorption spectra, a blue shift is observed in the absorption peak from 722 nm to 575 nm with the decrease in NCs size (average) from 43.0 nm to 8.2 nm.

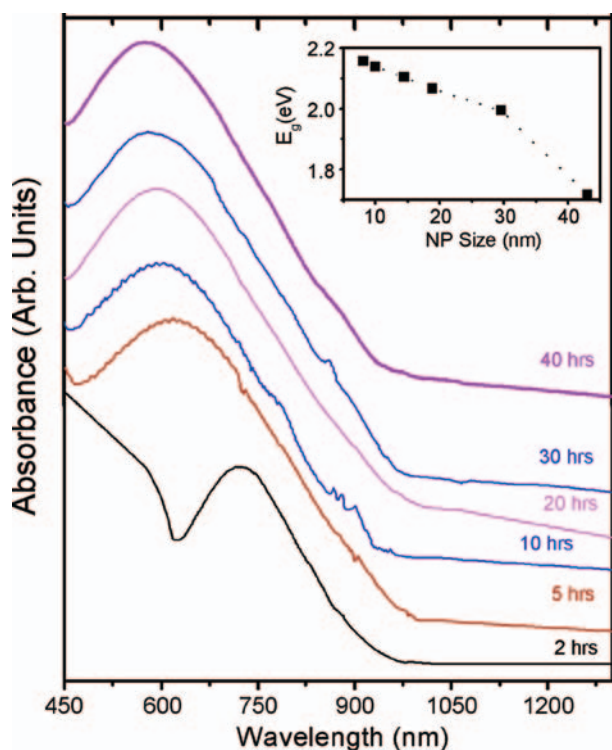


Fig. 5. UV-Vis-NIR absorption spectra of the different size Si NCs. Inset shows the blue shift of absorption energy with decrease in particle size (as calculated from Fig. 3).

The observed blue shift is a clear indication of the bandgap widening of the NCs, as shown in the inset of Figure 5. Since the excitonic Bohr diameter of Si is ~ 9.8 nm, the Si NCs obtained after 30 hrs and 40 hrs milling have sizes in a range where a quantum confinement effect is expected.¹⁷ However, we observed a systematic blue shift for all the NCs with size ranging from 5–45 nm. Therefore, the observed systematic blue shift cannot be attributed to the quantum confinement effect alone, if strain effects are ignored. For example, 30 nm Si NCs show visible absorption peaked at 2.0 eV where size effect is unlikely to be responsible for the band-gap widening to such an extent. Hence, lattice strain must strongly influence the band structure and it is most likely responsible for the observed change in the band structure. Thean et al. theoretically calculated the band gap widening of Si NCs as a function of strain⁶ and showed that the coupling between the Si NC geometry and the symmetry generated by the strain potential can enhance confinement in the quantum dot and can lift the degeneracy of the conduction band valleys for nonspherically symmetric NCs. In the present case, many of the anisotropically strained Si NCs are nonspherical, as seen from HRTEM image. Hence, strain induced enhancement of confinement is believed to be responsible for the band gap widening to the visible wavelength for the as-prepared Si NCs that show distinct absorption peak in the visible region.

3.4. Photoluminescence Studies

Room temperature PL spectra of the Si NCs suspended in methanol were recorded with the excitation wavelength 480 nm. The 30- and 40-hours ball-milled Si NCs show PL emission band in the visible region at 585 and 580 nm, respectively, as shown in Figure 6. No visible light emission was detected from the Si NCs with sizes above 10 nm, although these NCs show distinct absorption band in the visible region. The emission peak for the 40 hours milled Si NCs is blue shifted from 585 to 580 nm and the peak intensity is also enhanced compared to 30 hours samples. It is expected that PL emission from a single Si NC to be narrow, but in our case we observed a broad emission band. This peak broadening is caused by the size distribution as well as strain in the Si NCs. It is well known that electronic band gap has a power-law dependence to the crystallite size.¹⁸ Previously, Wilcoxon et al.¹⁹ reported PL peaks ranging from 1.8 to 3.6 eV for different cluster sizes from Si NCs colloidal suspension. In that case the intense violet peak was assigned to direct electron-hole recombination, whereas the less intense PL peak (~ 600 nm) was attributed to the surface state and phonon assisted recombination. Therefore, phonon assisted recombination is a likely candidate for the observed PL emission. However, the above mechanism cannot give rise to a strong emission at room temperature from the Si NCs. Similarly,

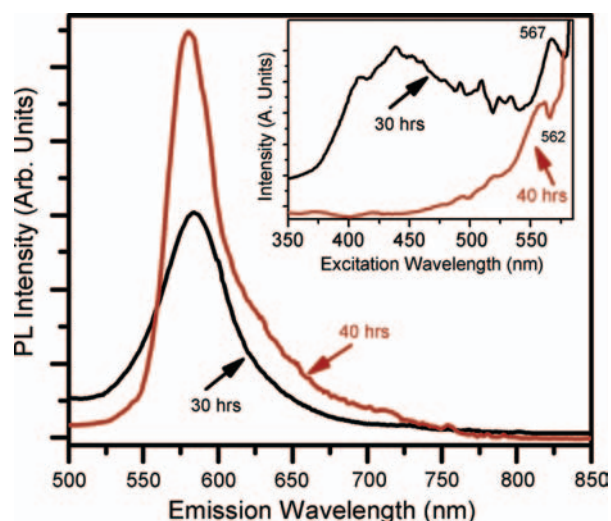


Fig. 6. Room temperature PL spectra of 30 and 40 hours milled Si NCs. Both the samples show strong emission in the visible region with peaks at 585 and 580 nm for the 30 and 40 hrs milling, respectively. Inset shows the PL excitation spectra of the Si NCs for the respective emission band.

contribution of defects or Si suboxide on the surface of the Si NCs can be other possible sources of the visible emission. However, surface defects/Si suboxides may be present on all size NCs, but NCs of size >10 nm did not show any visible emission, even though it showed distinct visible absorption band. Hence, surface defects/oxides are unlikely to be responsible for the observed visible PL emission.

To understand further the nature and origin of the visible PL, we performed PL excitation measurement for these two samples at their corresponding emission wavelengths, which is shown as inset of Figure 6. 30 hrs and 40 hrs milled Si NCs show excitation peaks at 567 and 562 nm, respectively that are close to the emission band. Note that 30 hrs milled Si NCs show an additional broad peak at 440 nm. We find that in both cases, calculated Stoke shift between absorption and emission band is very small (~ 0.067 eV). This small shift rules out the involvement of defects or interface states being responsible for the observed visible PL. This may indicate a direct transition from valence band to conduction band being responsible for the observed emission band from the Si NCs. We believe that due to the combined effect of strain and size, the band structure is modified for the strained Si NCs. We anticipate a quasi-direct energy gap with high oscillator strength for the strained Si NCs, resulting in visible light emission at room temperature. Fojtik et al.¹⁷ also reported the blue–green to red–orange emissions from colloidal suspension of Si NCs with different sizes. They attributed the luminescent mechanism is due to strong quantization of electronic levels in small size NCs, where free electron-hole recombination takes place in a very fast manner because of quasi-direct nature of transition. Therefore

it is expected that, quasi-direct transitions in the modified energy bands of the strained Si NCs is responsible for room temperature light emission in the green–yellow region.

Note that in the present study, no visible PL emission was observed from the higher diameter (>10 nm) Si NCs that are equally or even higher strained. We have shown from XRD and HRTEM analysis that strain steadily increases for milling time up to 10 hrs and it remains high for 20 hrs milled NCs. Thereafter, both the strain and NC size reduces for higher milling time. It is quite likely that due to high density of dislocations (screw type) associated with high strain in these NCs, the PL emission is inhibited by the nonradiative recombination centre associated with the dislocations in the Si NCs. Extended defects such as dislocations usually act as a non-radiative recombination centre in Si²⁰ and other semiconductors.²¹ Hence, despite the high band gap and visible absorption exhibited by these higher size Si NCs, nonradiative recombination centres trap the carriers and does not allow any visible emission from these NCs at room temperature. However, these NCs may exhibit visible PL emission at low temperature of measurement. Thus, an optimization of strain is essential to engineer the light emission from strained Si NCs. The present study shows the potential of strained Si NCs in engineering the PL from Si NCs in realizing the goals of Si based nanophotonics.

4. CONCLUSIONS

We have synthesized ultra fine and freestanding Si NCs with size down to ~ 5 nm using a simple ball-milling method and systematically investigated the strain evolution and changes in optical properties of the strained Si NCs as the function of milling time. The XRD line profile analysis enable proper estimation of crystallite size and nature of the strain. Our studies reveal that nature of the strain is anisotropic and the screw type dislocations are the main contributors to the lattice strain. The dislocation density and corresponding strain changes non-monotonically, while the crystallite size changes monotonically with milling time. Observed enhanced absorption in the visible region and a systematic blue shift in absorption peak with size reduction are believed to be due to the formation of wide quasi-direct energy bands in the Si NCs caused by combined effect of lattice strain and quantum confinement. The observed strong visible PL emission at room temperature supports the idea of quasi-direct energy bands formation in the strained Si NCs. We argued that the anisotropic strain in the small Si NCs is responsible for enhanced confinement effect for carriers that give rise to quasi-direct energy gap in Si. These results demonstrate the experimental evidence of combined effect of strain and quantum confinement effect to the optical properties of the freestanding strained Si NCs.

References and Notes

1. Y. D. Glinka, S. H. Lin, L. P. Huang, Y. T. Chen, and N. H. Tolk, *Phys. Rev. B* 64, 5421 (2001).
2. G. Ledoux, O. Guillois, D. Porterat, C. Reynaud, F. Huisken, B. Kohn, and V. Paillard, *Phys. Rev. B* 62, 15942 (2000).
3. X.-H. Peng, S. Ganti, A. Alizadeh, P. Sharma, S. K. Kumar, and S. K. Nayak, *Phys. Rev. B* 74, 035339 (2006).
4. C. Delerue, M. Lannoo, and G. Allan, *Phys. Rev. Lett.* 84, 2457 (2000).
5. D. M. Lyons, K. M. Ryan, M. A. Morris, and J. D. Holmes, *Nano. Lett.* 2, 811 (2002).
6. A. Thean and J. P. Leburton, *Appl. Phys. Lett.* 79, 1030 (2001).
7. X. L. Wu and F. S. Xue, *Appl. Phys. Lett.* 84, 2808 (2004).
8. L. Seravalli, M. Minelli, P. Frigeri, P. Allegri, V. Avanzini, and S. Franchi, *Appl. Phys. Lett.* 82, 2341 (2003).
9. C. Li, Y. Chen, Z. Zhou, H. Lai, and S. Chen, *Appl. Phys. Lett.* 95, 251102 (2009).
10. G. K. Williamson and W. H. Hall, *Acta Metall.* 1, 22 (1953).
11. T. Ungar and A. Borbely, *Appl. Phys. Lett.* 69, 3173 (1996).
12. T. Ungar, I. Dragomir, A. Revesz, and A. Borbely, *J. Appl. Crystallogr.* 32, 992 (1999).
13. L. C. Damonte, L. A. M. Zelis, B. M. Soucase, and M. A. H. Fenollosa, *Powder Technol.* 148, 15 (2004).
14. T. D. Shen, I. Shmagin, C. C. Koch, R. M. Kolbas, Y. Fahmy, L. Bergman, R. J. Nemanich, M. T. McClure, Z. Sitar, and M. X. Quan, *Phys. Rev. B* 55, 7615 (1997).
15. D. R. Lide (Ed.), *CRC Handbook of Chemistry and Physics* (Taylor and Francis, Florida), 89th edn., Internet Version (2009), pp. 12–34.
16. P. K. Giri, *J. Phys. D: Appl. Phys.* 42, 245402 (2009).
17. A. Fojtik and A. Henglein, *J. Phys. Chem. B* 110, 1994 (2006).
18. T. Takagahara and K. Takeda, *Phys. Rev. B* 46, 15578 (1992).
19. J. P. Wilcoxon, G. A. Samara, and P. N. Provencio, *Phys. Rev. B* 60, 2704 (1999).
20. V. Higgs, F. Chin, X. Wang, J. Mosalski, and R. Beanland, *J. Phys.: Condens. Matter* 12, 10105 (2000).
21. M. Albrecht, J. L. Weyher, B. Lucznik, I. Grzegory, and S. Porowski, *Appl. Phys. Lett.* 92, 231909 (2008).

Received: 26 June 2010. Accepted: 22 December 2010.